Characterization and modelling of Al and Cu busbar during charging and discharging of Li-ion battery for electric vehicles

Omkar Mypati[1], Tariq Anwaar[2], Desham Mitra[3], Surjya Kanta Pal[1*], Prakash Srirangam[4]

[1] Department of Mechanical Engineering, Indian Institute of Technology Kharagpur, 721302, India

[2] Department of Mechanical Engineering, National Institute of Technology Tiruchirappalli, 620015, India.

[3] Department of Electrical Engineering, Indian Institute of Technology Kharagpur, 721302, India

[4] Warwick Manufacturing Group, University of Warwick, CV4 7AL, UK

Corresponding author: skpal@mech.iitkgp.ac.in

Abstract

The electrical components such as bimetallic busbar joints of the lithium-ion (Li-ion) batteries should be able to withstand high voltages during charge and discharge processes. The busbar is an essential component that transmits high power to electrify the vehicle. The present study describes the sustainability of friction stir welded (FSW) busbar at different C-rates by simulating a Li-ion battery attached to a busbar, then correlating the heat generation of simulation results with an experimental result at 1, 1.5, and 2C-rates. The change in process parameters of FSW samples varies with electrical conductivity at the weld interface. The variation in electrical conductivity with different busbars is due to the formation of various intermetallic and changes in the grain size of the Al and Cu joints. However, the busbar with Cu-rich intermetallic exhibits smaller electrical resistivity. The specific electrical contact resistance of a busbar is obtained from simulation by validating the heat generated during constant time charge-discharge cycles. The temperature rises due to contact resistance in the Al-Cu busbar which can lead to thermal runaway and, eventually, short circuits in the Li-ion battery pack. Based on previous simulation parameters, the Li-ion cells are simulated at 5 and 10C-rates to understand thermal runaway behaviour.

Keywords: Friction stir welding, Busbar, Li-ion battery, electric vehicles, intermetallics, contact resistance

NOMENCLATURE

$\nabla \vec{\imath}$ linear current density vectors

J Current density

Ω_P positive domain of a Li-ion cell electrode

Ω_n negative domain of a Li-ion cell electrode

r_p resistance of positive electrode

r_n resistance of negative electrode

v_p potential of positive electrode

v_n potential of negaive electrode

Q_t theoretical capacity

C_p volume-average specific heat capacity under constant pressure

C NTGK model constant

T temperature

k_i respective thermal conductivities along the X, Y, and Z directions

q heat generation rate per unit volume

E_{0C} open circuit potential

E cell voltage

a specific area of the battery

a_p specific area of the positive electrodes

a_n specific area of the negative electrodes

q_{conv} heat dissipation rate

h convection heat transfer coefficient on the battery

d battery thickness (perpendicular to the electrodes)

T_{air} atmospheric temperature.

1 Introduction

Today, electric vehicles (EVs') have gained popularity because of their high efficiency, minimum CO_2 emissions, low noise, and low maintenance requirements compared to internal combustion engines (ICs) [1,2]. The main types of EVs' are battery-electric vehicles (BEVs') and hybrid electric vehicles (HEVs'), etc. The batteries power the electric motor of a BEV, and the speed requirements vary using a controller [3]. Furthermore, the controller in BEVs' regulates the motor's output torque. Both an electric motor and an internal combustion engine power the HEVs', where the electric motor serves as a supplement. Batteries provide power at low speeds to achieve a high torque in a small time. Due to the EV's limited battery capacity and maximum speed, the IC engine takes over when it reaches high speeds in HEVs' [4]. The busbar is the main component of the battery pack, where it transmits electricity between Li-ion cells to generate the power needed to run the EV. Busbars are used to transfer high current over short distances [3,5–8]. The busbar was initially made of Cu due to its high electrical conductivity, i.e., 5.87×10^7 S/m [9]. However, because of its lower price, smaller weight, and comparative electrical conductivity values, Al alloys are increasingly being used. Therefore, the traditional Cu busbar is replaced with an Al-Cu busbar [10]. Al has a higher thermal expansion coefficient than Cu. A high thermal expansion rate and oxidation of the Al further degrades the electrical connections. In addition, the connection of Al busbars with anode current collectors is complicated due to their different material combinations [11]. The use of bimetallic busbars made from Al and Cu could be a potential solution to this problem. Many researchers have fabricated a variety of busbars using different welding techniques like resistance spot welding, ultrasonic welding, press contacts and laser beam welding [12–14]. Even though Al-Cu joints are produced by fusion welding, which is challenging due to the difference in fusion temperatures for Al and Cu. it is not a concern for friction stir welding (FSW) [15–17]. The critical issues in the FSWed busbar, like varying deformation behaviour at different zones and formation of intermetallic compounds (IMC) at lower temperatures, influence the joint and electrical properties. IMC refers to a solid phase containing two or more metallic elements and at least one non-metallic element with a crystal structure distinct from the rest of its composition. In this regard, friction welding of Al and Cu results in the formation of AlCu and Al_2Cu IMC [18–20]. The formation of thicker IMC layers negatively affects the electrical resistivity. Hence the observed electrical resistivity for the IMC thickness 21 μm and 107 μm IMC layer is 45 μΩ cm and 85 μΩ cm, respectively [21]. Higher IMC layer thickness increases electrical resistivity, leading to a rise in heat when a current passes through it. In

order to determine the thermal behaviour of the Li-ion battery attached to an FSWed busbar, the authors performed a detailed literature review of the simulation of the battery using different models, detailed below.

Li-ion cells can be represented using various electrical, mathematical, and electrochemical models, which have been briefly explained [22]. The electrical model is described as a circuit that consists of the equivalent circuit model (ECM) [23]. ECM components are ideal voltage sources that correspond to the open-circuit voltage. The series resistance of a battery corresponds to its ohmic resistance when applied at a constant C-rate. The R-C circuit represents the dynamic conditions of the model. The dynamic nature of batteries results in various effects like the nonlinear open-circuit voltage, calibration issues, time-dependent storage capacity, transient response, and more, posing a great challenge to developing accurate BMS [24]. Hence the ECM model represents a trade-off between accuracy and computation efficiency [23,25,26]. Mathematical models require small computational power. One parameter of the mathematical model of the electrical battery is used to approximate the battery state of health (SoH). Stochastic methods are used, which deal with the uncertainties involved in charge recovery mechanisms during pulse discharge of batteries. However, these methods do not provide information about the current-voltage relationship, which is important for optimising the battery system. The electrical parameter is then calculated from the constant current constant voltage charge (CC-CV) curve [27]. Therefore, an expression is developed for the current during each charge cycle. Additionally, analytical models employ simple equations capable of predicting the nonlinear relationship between charging-discharging rate and battery capacity. However, one of the biggest disadvantages of analytical models is that battery parameters can differ from one another even if they are of the same dimensions and geometry. These analytical models predict the load frequency for which the charge delivered is highest for a particular value of load and battery parameters. Hence the battery lifetime predictions cannot be used even for batteries with similar geometry [28]. An electrochemical model is used to simulate Li-ion flow for different C-rates of a Li-ion cell. Models relate macroscopic characteristics such as voltage and current of the battery to microscopic characteristics such as active cell material and concentration distribution. Therefore, such models dive deeply into the mechanisms of the battery and are highly accurate [24]. There is a time-varying partial differential equation relating the parameters, and there have been studies recently which have made this method computationally effective [29]. However, one of its disadvantages is since

the model has a significant number of unknown parameters, overfitting is a problem, contributing to poor model robustness [29,30].

The 3D modelling of Li-ion batteries is efficiently represented using an electrochemical model, i.e., Newman, Tiedeman, Gu, and Kim (NGTK) model, developed by Kwon et al. [31]. The main advantages of this model are ease of parameter adjustment to match for the validation and the least computational demand compared to other electrochemical models like the Newman pseudo-two-dimensional (P2D) model. In contrast, Li et al. introduced a computationally-efficient P2D model using a reduced-order Li-ion battery simulation where the solution depends on matrix algebra. Additionally, the ODE-based system resolves the physics-based Li-ion cell modelling with a more efficient and accurate method by eliminating the algebraic equations that require iterative solutions [32]. However, the NGTK model simulates various kinds of cathode materials used in Li-ion batteries. A Li-ion cell has been modelled using NGTK containing a cathode of LiFePO$_4$, an anode of graphite, and an electrolyte. The study validated the discharge curves of the experiment with the modelling results, where the discharge rates ranging from 0.5 to 5C-rates was calculated. According to modelling results of potential and current density distributions, heat generation rates are calculated based on discharge time and electrode position to predict temperature distributions of Li-ion cells. The maximum temperature obtained during 1, 3, and 5C-rates were 299.5 K, 306 K, and 317.7 K, respectively, at an ambient temperature of 300 K [33]. In another literature, a LiFePO$_4$ pouch type battery is experimentally and numerically analyzed for discharge rates of 1C-rate to 5C-rate at an ambient temperature of 300 K subjected to naturally convective conditions. The experiments are carried out at a high discharge of 5C-rate, for which a temperature of 325.2 K has been observed during the natural convection cooling. Accordingly, the study developed a correlation equation of the heat transfer rate through the battery surface at 11.5 W for 5C-rate discharge [34]. Based on this literature, the heat generation in the Li-ion cell during a charge-discharge depends on C-rate and the ambient environmental temperature.

Moreover, all the literature study focuses on the experimental performance of Li-ion batteries at different C-rates and is further validated with the simulation results. There was no substantial literature on the busbar attached with a Li-ion battery. Hence, the present study details the application of an effective FSWed Al-Cu busbar to a Li-ion battery pack. The FSW busbar has advantages over other welding techniques in the perspective of mechanical and electrical properties. The effectiveness of the FSW Al-Cu busbar is studied by attaching it to a Li-ion

cell and subjected to a different C-rate. The temperature during different C-rates is measured at the joint interface of the busbar. In addition, the whole experimental system is modelled with the same C-rate, and the temperature contours have been validated with the experimental results to determine the specific contact resistance between the Al and Cu in the busbar. Eventually, the contact resistance is validated by measuring the electrical resistance of the busbar using a 4-probe electrical conductivity setup. The need for fast charging in EVs', the Li-ion battery pack in EVs' is subject to higher C-rates. Consequently, the system is further modelled with the specific contact resistance at 5 and 10C-rate, making it impractical to perform an experiment due to failures and thermal runaway in the Li-ion cell and busbar.

2 Experiment and characterization procedure

A linear FSW machine (WS004, ETA Bangalore) is used to fabricate the Al-Cu busbar. An Al of 1mm thickness is placed over a 2mm thickness Cu. H13 tool steel is used for welding the Al and Cu, which has a shoulder diameter of 16 mm, a pin diameter of 5 mm, and a pin height of 1 mm. The process parameters of the welding are listed in Table 1.

Table 1. Process parameters used to fabricate an Al-Cu busbar using FSW

Sample	Tool rotational speed (ω)	Welding speed (v)	Tilt angle (degrees)	Plunge depth (mm)	Grain size (μm)	Micro-hardness (HV)
S$_1$	1600	60			4.92	256
S$_2$	2400	60	2	0.2	8.67	227
S$_3$	2400	120			7.85	238

As shown in Figure 1, this study uses an Al-Cu busbar attached to a Li-ion cell to investigate the characteristics of the busbar when the cell is subjected to different C-rates. The cell parameters have been presented in table 2. The cathode of A123 type pouch cell is attached to the positive terminal of a battery cycler (Biologic, BCS-800), using a mono-channel pouch cell clamp (Biologic, PBH-150). A nonconductive industrial holding clip is used between the busbar and tab of the Li-ion battery to hold the cell and busbar in place. The Cu-side of the busbar is clamped to an anode of the cell. The Al-side of the busbar is clamped to the negative terminal of the cycler. During the charge-discharge experiments, an ambient temperature of 301 K is maintained inside a chamber. Furthermore, the voltage has been measured on the terminals, where the effect of the weld interface has been determined.
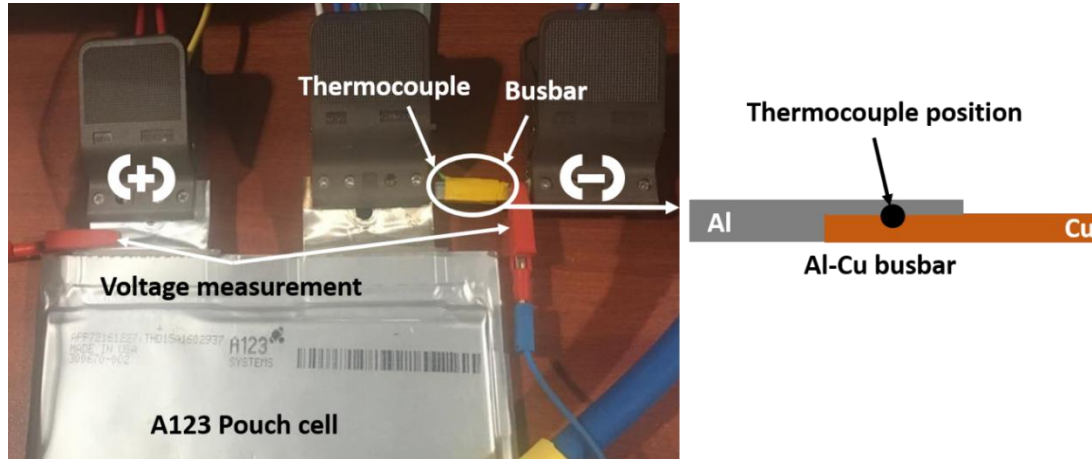
Figure 1. Experimental setup attaching an Al-Cu busbar with the A123 pouch cell

Table 2. Li-ion cell specifications

Parameters	Values
Cell type	Pouch cell (A123 System)
Cell weight	496 g
Cathode Material	$LiFePO_4$
Anode Material	Graphite
Electrolyte material	Carbonate based
Energy content	65 Wh
Specific power	2400 W/kg
Nominal capacity	19.6 Ah
Nominal voltage	3.3 V
Cut-off discharge voltage	2V
Energy density	247 Wh/L

X-ray diffraction techniques (PANalytical B.V, 7602 EA) have been used to identify the IMCs at the interface by utilizing a Cu anode source and maintaining a current of 40 mA within the range of 20 ° to 130 °. The electrical resistivity of the FSWed samples is measured with a 4-probe electrical conductivity setup (Ecopia, 0.545T) to validate the contact resistance. In order to validate the electrical resistivity, the microstructure of the welded samples is found using an electron back-scattering diffraction (Zeiss, Merlin) analysis.

3 Simulation details

3.1 Geometry and setup

Computational fluid dynamics (CFD) simulations (Ansys, 2021) have been used In order to study the heat generation during the electrochemical process of the Li-ion cell attached to a busbar using temperature contours. The electrochemical processes refer to capturing the chemical reactions in the anode and cathode of the cell during charge and discharge processes through electrochemical models like the Newman, Tiedemann, Gu, and Kim (NTGK) semi-empirical model. The 3D geometry of an A123 prismatic pouch battery is constructed according to the datasheet, and the dimensions of the active material are 160 mm (length), 227 mm (width), and 7.25 mm (thickness). The dimensions of the current collectors or tabs are given as 45 mm (length), 15 mm (width), and 7.25 mm (thickness). The simulation is based on the fact that the positive and negative tabs of the Li-ion battery are made of aluminium, and copper, respectively. In Table 3, the material properties are shown as input to the simulations for the electrolyte region, the positive tab region, and the negative tab region. In the present simulation, the electrode cell volume is taken into account, i.e., positive electrode 1.85 % and negative electrode 1.85 % of the total cell volume. The nominal cell capacity is set as 19.6 Ah. In addition, the specific contact resistance at the junction of the Al-Cu busbar is also modelled, further correlated with the experimental result. As part of the fluent setup, the energy and multiscale multidomain (MSMD) battery models are activated, and the NTGK model is selected for the Li-ion battery analysis [35,36]. As energy is constantly converted from one form to another during the process of charging and discharging, hence by activating the energy model which allows mass, momentum, and energy conservation. Following the formulation of the energy conservation equation for a single cell, the mass, momentum, and energy equations are discussed in later sections. The MSMD is activated to generate a three-dimensional electrothermal model based on the input data. Next, using the profile setting, a time-dependent input is given through the time-scheduled option defining parameters like the C-rate, current, voltage, and power. For this study, the parameters used to describe the battery chargings are the C-rate and the time. The input "0 -1 0 500 -1 0" provided in the simulation implies that the battery is charged at a constant rate of 1C for 500 seconds. These details are stored in an ASCII text file, which has been provided to the simulation. The voltage range of 3.6 V and 2 V is specified for the maximum and minimum stop voltages. Additionally, three different resistances are applied to the contact area between the Al and Cu of a busbar for the three different cases, which are also experimentally verified. In order to validate and verify the simulation results, grid independence studies are conducted by systematically increasing the

mesh size from 1mm to 10mm. Initial mesh refinement improved the accuracy of the solutions, but they eventually became constant. As mesh refinement progressed, the time needed to compute solutions also increased exponentially. The heat generation on the battery and the busbar is measured by a highly accurate temperature reading option (surface monitor) in the post-processing setup of Ansys software during a simulation at C-rates of 1C, 1.5C, and 2C.

Table 3. Material properties of electrolyte and tabs of the Li-ion battery

Property	Electrolyte Region	Positive Tab (Al)	Negative Tab (Cu)
Density (kg/m^3)	2092	2800	8910
Specific Heat Capacity (J/kgK)	871	910	390
Electrical Conductivity (W/mK)	202.4	245	375

3.2 Assumptions

1. Convectional heat transfer is considered on the surfaces of the battery and the tabs. Radiational heat transfer is ignored in the current study.
2. Specific contact resistances between the Al-Cu are taken from the conductance values.
3. The initial condition is that the battery has a uniform and homogeneous temperature distribution, equivalent to a temperature of 300K.
4. Properties like the heat transfer coefficient and the thermal conductivity are taken to be constant throughout the material and independent of temperature changes

3.3 NTGK model

Modelling of the Li-ion battery with the Al-Cu busbar is implemented using an NTGK model. The NTGK model is a simple semi-empirical electrochemical model. In this model, 2 polarisation expressions are developed for the positive and negative electrodes [37]. In the model formulation, the volumetric current transfer rate is related to the potential field of the electrodes. For a given battery, the voltage-current response curve can be obtained through experimentation. The U and Y parameters can then be determined by curve fitting the data

using Ansys Fluent's in-house parameter estimation function. The battery temperature and heat generation rates due to electrochemical heating are calculated with the help of solving the Navier-Stokes equations including mass, momentum, and energy terms. Afterwards, the energy conservation of a single cell is formulated, followed by the mass, momentum, and energy equations. The following section outlines the governing equations, boundary conditions, and assumptions used during the simulations.

3.4 Governing equations

Equations 1 and 2 are the continuity equation for the positive and negative tab regions, respectively [31];

$$\nabla \vec{\iota_p} - J = 0 \ (\Omega_P) \tag{1}$$
$$\nabla \vec{\iota_n} + J = 0 \ (\Omega_n) \tag{2}$$

where $\nabla \vec{\iota}$ is linear current density vectors, J is Current density (A/m^2), Ω_P and Ω_n are the domains of a Li-ion cell positive and negative electrodes, respectively.

From Ohm's Law, Equations 3 and 4 are derived for the positive and negative tab regions, respectively [31];

$$\vec{\iota_P} = -\frac{\nabla v_p}{r_p} \tag{3}$$

$$\vec{\iota_n} = -\frac{\nabla v_n}{r_n} \tag{4}$$

where r_p is the resistance of a positive electrode, r_n is the resistance of a negative electrode. v_p and v_n refer to the potentials of the positive and negative electrodes, respectively

Combining Equations 1, 2, and 3, 4, the expressions for the linear current density vectors of the positive and negative tabs are given in Equations 5 and 6, respectively [38];

$$\nabla^2 v_p = -r_p \, J \tag{5}$$
$$\nabla^2 v_n = +r_n \, J \tag{6}$$

The corresponding volumetric current transfer density (J) of Equations 5 and 6 is a function of the potential difference between the positive and negative electrodes. This functional form

depends on the polarisation characteristics of the electrode. The polarisation parameters are considered and are given in Equation 7 [37];

$$J = Y(v_{\mathrm{p}} - v_n - U) \tag{7}$$

where $(v_{\mathrm{p}} - v_n)$ represents the change in potential between the positive and negative electrodes. *U* & *Y* are expressed as a polynomial function of the Depth of Discharge (DoD), as given in Equations 8 and 9, respectively [39];

$$U = \sum_{n=0}^{3} a_{\mathrm{n}}(\mathrm{DoD})^{\mathrm{n}} - C_1(T - T_{\mathrm{ref}}) \tag{8}$$

$$Y = \sum_{n=0}^{6} b_{\mathrm{n}}(\mathrm{DoD})^{\mathrm{n}} \exp[-C_2(\frac{1}{T} - \frac{1}{T_{\mathrm{ref}}})] \tag{9}$$

The constants a_0 to a_3 and b_0 to b_5 are calculated through numerical methods. A linear or polynomial parameter estimation approach has not been used in this study. Consequently, the constant values are estimated using the trial-and-error method since there is no direct relationship between the cell voltage and the constants values. According to Table 4, the values of the constants are taken to caliculate the *U* and *Y* function [34,40].

Table 4. The constant values of the *U* & *Y* function

Parameter	Value
a_0 (V)	3.6
a_1 (V)	-0.804
a_2 (V)	1.075
a_3 (V)	-1.177
b_0 (A/m^2)	1168.6
b_1 (A/m^2)	-8928
b_2 (A/m^2)	5.25×10^4
b_3 (A/m^2)	-1.3×10^5
b_4 (A/m^2)	1.58×10^5
b_5 (A/m^2)	-6.758×10^4

Under model parameters tab in Ansys fluent set-up, parameters like the reference capacity, initial DoD and other coefficients are defined. Since the simulation begins with a charged battery, the DoD is set to 0.1. The expression for the DoD is given in Equation 10;

$$\text{DoD} = \frac{1}{Q_\text{t}} \int_0^t (J) \, \mathrm{d}t \tag{10}$$

where Q_t represents the theoretical capacity of the battery per unit area of the electrodes, and t is the discharge time.

In the Ansys Fluent module, heat generation rate and battery temperature are governed by Navier-Stokes equations, which include mass, momentum, and energy conservation, based on the application. Hence based on the differential conservation of energy in a battery, the 3-D transient equation for heat conduction can be written as given in Equation 11 [41];

$$\rho C_\text{p} \frac{\partial T}{\partial t} = \frac{\partial}{\partial x} \left(k_\text{x} \frac{\partial T}{\partial x}\right) + \frac{\partial}{\partial y} \left(k_\text{y} \frac{\partial T}{\partial y}\right) + \frac{\partial}{\partial z} \left(k_\text{z} \frac{\partial T}{\partial z}\right) + q \tag{11}$$

where C_p represents the volume-average specific heat capacity under constant pressure, ρ represents the density, T represents temperature, and k_i the respective thermal conductivities along the X, Y, and Z directions. Here, q refers to the heat generation rate per unit volume. The heat generation rate in the battery and tab region q, given in the above Equation 11, is expressed in Equation 12 [42];

$$q = J \left\{ U - (v_\text{p} - v_\text{n}) - T \frac{\mathrm{d}U}{\mathrm{d}T} \right\} + \frac{a_\text{p} \nabla^2 v_\text{p}}{r_\text{p}} - \frac{a_\text{n} \nabla^2 v_\text{n}}{r_\text{n}}, \tag{12}$$

where a_p and a_n are the specific areas of the positive and negative electrodes, respectively. Equation 12 represents the charge transfer in the electrode-electrolyte interface with reversible and irreversible terms. The irreversible term refers to energy loss due to the difference between cell potential and open circuit potential due to electrochemical polarisation. The reversible part refers to the entropy change. Further, the ohmic heating in the positive and negative electrodes is also determined as the last two terms, respectively.

3.5 Boundary equations

Next, the q_{conv} term refers to the heat dissipation rate and is derived as shown in the Equation 13 [41,42], where a convective boundary condition is applied on the boundaries of the electrode;

$$q_{conv} = \frac{2h}{d}\ (T\ - T_{air})$$
(13)

where h (W/m^{2}K) represents the convection heat transfer coefficient on the battery, d specifies the battery thickness (perpendicular to the electrodes), and T_{air} refers to the atmospheric temperature. The heat transfer coefficient is found using the Nusselt number and Rayleigh number [34]. The heat transfer coefficient value used for the simulation is 12.5 W/m^{2}K for natural convection conditions at 300K ambient temperature.

4 Result and discussions

4.1 Validation of simulation and experimental results

The temperature contours on the system (Li-ion cell attached with busbar) are recorded at 1, 1.5, and 2C-rate. Initially, the charged Li-ion cell is discharged for 20 min at 1C-rate, followed by 20 minutes of cooling. Next, the battery is charged at 1C-rate for 20 minutes and again cooled for 20 minutes. Similarly, the experiment for other C-rates of 1.5 and 2C are conducted. Figures 2 and 3 are the temperature contours of a Li-ion battery corresponding to the end of the 20 min discharge and charge, respectively. The temperature rise during the simulation is due to the internal resistance of the Li-ion cell and welded samples while charging and discharging. The simulations are performed by varying the specific contact resistance between Al and Cu in the busbar. Contact resistance is determined by correlating the temperature contour with both simulation and experimental results. A variation in process parameters affects the composition of intermetallic compounds and the grain size at the weld interface of the busbar, which also affects the resistance at the weld interface. According to Figures 4 (a), (b), and (c), as the resistance varies, the heat generated at the interface changes. By varying the contact resistance of the joint used in the simulation, the experimental temperature profile at the weld interface is compared with the simulation results. A contact resistance area of 16 mm x 10 mm at the weld nugget zone of the Al-Cu busbar is considered in the current simulation.
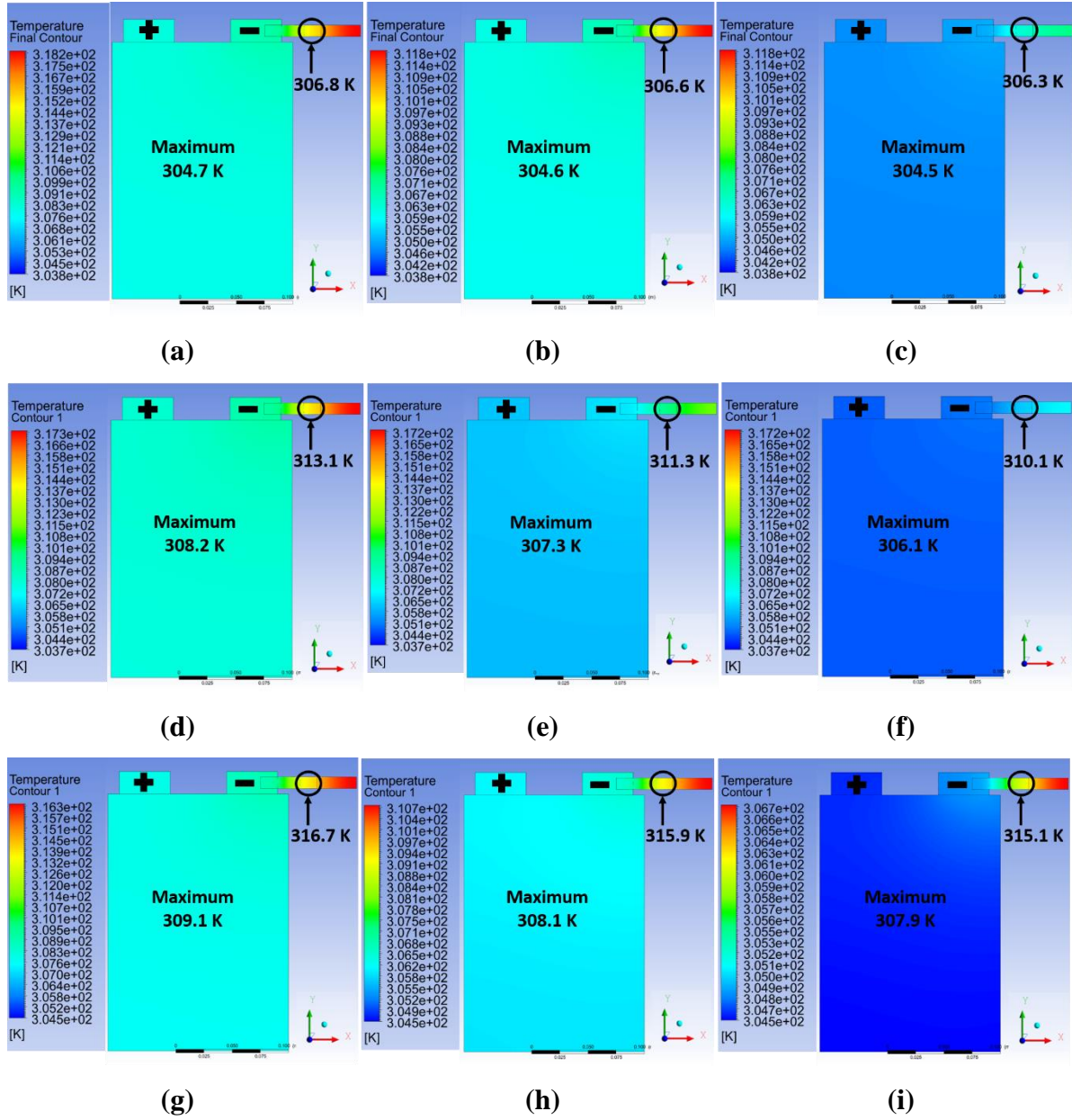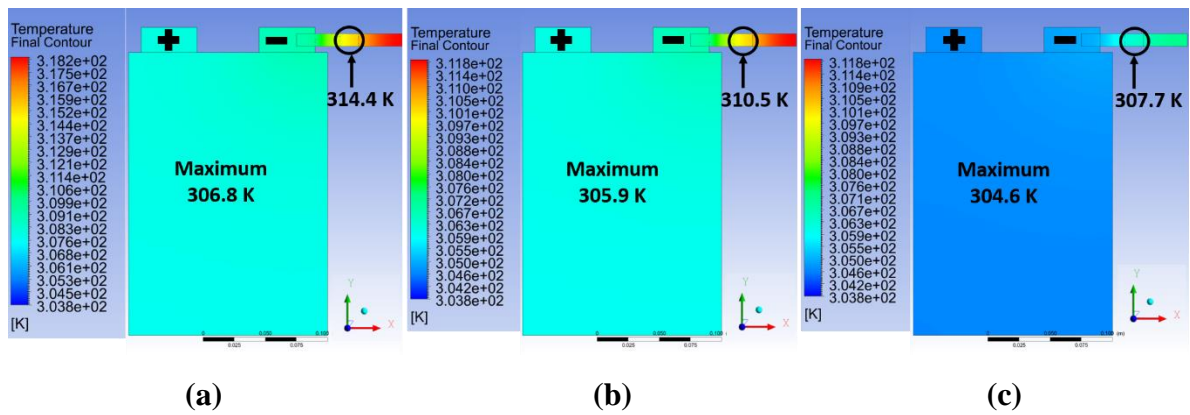
Figure 2. Temperature contours of Li-ion cell clamped with busbar during discharge state for sample S_1, S_2, and S_3 (a)-(b)-(c) 1C-rate, (d)-(e)-(f) 1.5C-rate, (g)-(h)-(i) 2C-rate, respectively

According to the simulation parameters, heat was generated at the weld interface of the busbar due to electrical contact resistance, which is further validated with the temperature profiles obtained from an experimental study for busbars S_1, S_2, and S_3. Thus, the specific contact resistances for the busbars S_1, S_2, and S_3 are determined to be $3\times10^{-8}\,\Omega\,m^2$, $2.7\times10^{-8}\,\Omega\,m^2$, and $2.5\times10^{-8}\,\Omega\,m^2$, respectively, during the simulation. Figures 2 and 3 illustrate the discharge and charge simulation contours at the end of 20 min at 1, 1.5, and 2C-rate, respectively. For a busbar with a specific contact resistance of $3\times10^{-8}\,\Omega\,m^2$, i.e., sample S_1, the maximum temperature

recorded during discharge for 1C-rate is 304.7 K on the Li-ion cell and in the busbar is 306.8 K, as shown in Figure 2 (a). Generally, at a lower C-rate, the movement of electrons is slower, due to this, a lower temperature is observed. For a 1.5C-rate, the maximum temperature recorded during discharge in the Li-ion cell is 308.2 K and in the busbar is 313.1 K, as shown in Figure 2 (d). The heat generation is slightly increased in both the Li-ion cell and the busbar. The busbar is conducting more heat from the li-ion cell. The maximum temperature recorded at 2C-rate during discharge in the Li-ion is 309.1 K and in the busbar is 316.7 K, as shown in Figure 2 (g), which is higher than the other C-rates. The increase in temperature regarding C-rate is caused by an increase in resistance of the busbar for fast-moving electrons, as mentioned earlier.

Similarly, for a specific contact resistance of $2.5 \times 10^{-8} \, \Omega \, m^2$, the maximum temperature during charging of the battery and busbar for 1C-rate is 304.6 K and 307.7 K, respectively, as shown in Figure 3 (c). The increase in contact resistance and the variation in the peak temperature generation are observed in both the Li-ion cell and busbar. For a 2C-rate, the maximum temperature during charging the battery and busbar was 304.9 K and 306.4 K, respectively, as shown in Figure 3 (i). Next, for a specific contact resistance of $3 \times 10^{-8} \, \Omega \, m^2$, the maximum temperature of the battery and busbar for 1C-rate charging was 306.8 K and 314.4 K, respectively, as shown in Figure 3 (a). For a 2C-rate, the maximum temperature of the battery and busbar was 310.4 and 313.2 K, respectively, as shown in Figure 3 (g).
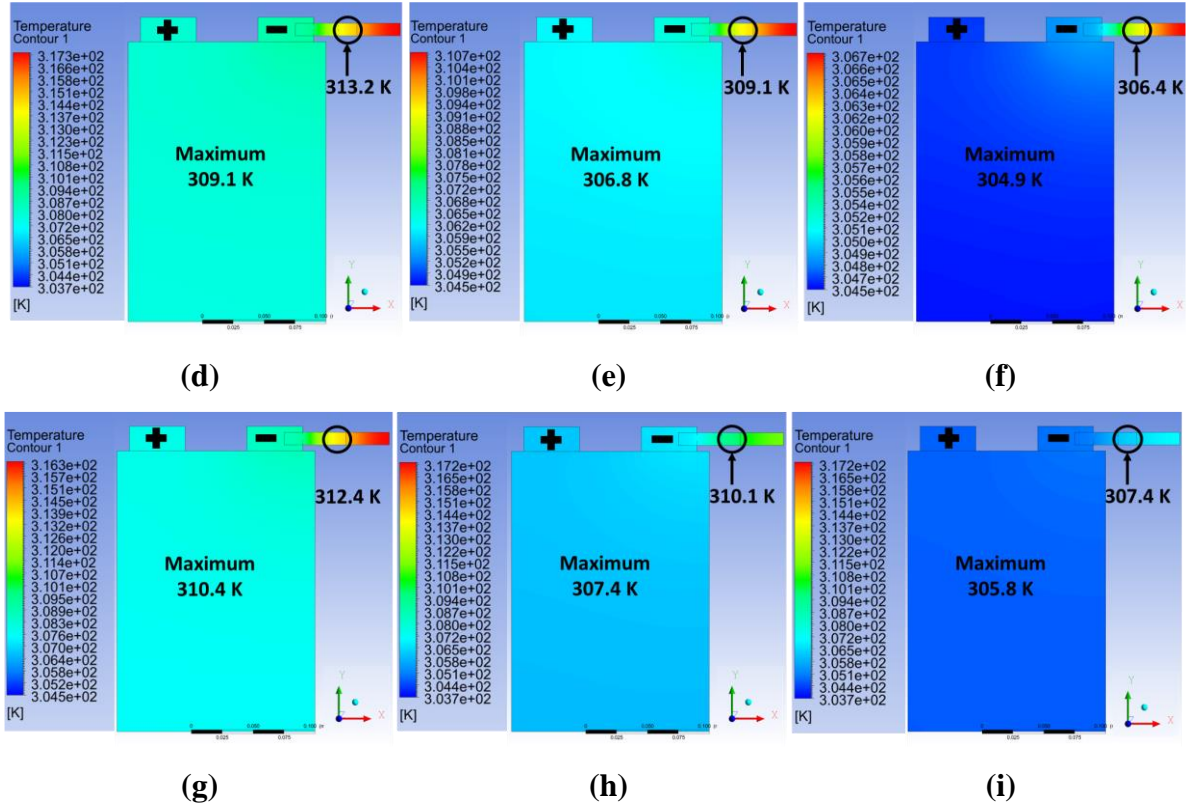

(a)   (b)   (c)

Figure 3. Temperature contours of Li-ion cell clamped with busbar during charge state for sample S_1, S_2, and S_3 (a)-(b)-(c) 1C-rate, (d)-(e)-(f) 1.5C-rate, (g)-(h)-(i) 2C-rate, respectively

In conclusion, a relation between specific contact resistance and the heat generation of the Li-ion cell and the busbar has been determined. There is a tendency that an increase in contact resistance leads to an increase in the peak temperature generation of the Li-ion cell and busbar [12–14]. Peak temperatures obtained at the Al-Cu busbar are higher than those generated at the Li-ion cell surfaces during different C-rates. The busbar acts as a heat conductive material in this particular system. The region of contact resistance is signified as a welding area of the Al-Cu busbar, which has been explained in later sections. By varying the contact resistance at the junction of the Al-Cu busbars, the temperature profile obtained from the simulation is validated with experimental temperature profile attained during the testing of busbars attached with Li-ion cell.

Temperature profiles at weld interfaces for different processed busbars are shown in Figures 4a, b, and c at 1C, 1.5C, and 2C-rates, respectively. As the C-rate increases, the temperature rises due to internal contact resistance in the busbar opposing faster moving electrons. However, the peak temperature of various busbars differs due to different IMC configurations present in the weld zone. A maximum temperature has been observed in sample

S$_1$, where the presence of Al-rich (A1$_2$Cu) IMC is illustrated in Figure 4d. Al-rich IMC is hard and brittle, which affects the mechanical and electrical properties of the busbar, thus increasing the temperature as they conduct current. The average microhardness in the nugget zone for sample S$_1$ is about 256 HV, even though base Cu is 95 HV. The sample S$_2$ consists of two major types of IMC, namely Al$_4$Cu$_9$ and AlCu. Among them, Al$_4$Cu$_9$ is Cu-rich and highly conductive. The average microhardness is found to be 227 HV. Therefore, the temperature generation is smaller during the application of different C-rates compared to S$_1$. Furthermore, the temperature fall during the holding time for sample S$_3$ is higher due to the presence of Al$_4$Cu$_9$ IMC. This IMC allows faster heat dissipation, which in turn allows for faster cooling within the busbar. Moreover, sample S$_3$ has a microhardness of 238 HV, which is higher than sample S$_2$. Generally, with an increase in microhardness, the electrical resistivity of the sample increases. This phenomenon is applicable for the higher hardness variation; however, the change in microhardness for samples S$_2$ and S$_3$ is very small. A significant correlation of electrical conductivity had not been observed between S$_2$ and S$_3$. Hence, microstructural changes in the samples were further studied and explained in later sections.

The simulation temperature profiles are superimposed on experimental data as shown in Figures 4a, b, and c. Based on the validation of the temperature profile, Table 5 shows the measured experimental electrical resistivity and the obtained contact resistance. Further, the magnitude of measured electrical resistivity and specific contact resistance are not the same, however, a similar decrease in trend is observed in busbars S$_1$, S$_2$ and S$_3$. The electrical resistivity of sample S$_1$ was measured to be 4.29×10^{-5} Ω cm. According to the simulation result, the specific contact resistance of sample S$_1$ is 3×10^{-8} Ω m^2. The electrical resistivity of sample S$_2$ is measured to be $3.44 \ 10^{-5}$ Ω cm, which is lower than that of sample S$_1$. The decrease in resistivity is due to the formation of Cu-rich IMC at the weld interface of the busbar. In addition, the average microhardness in the nugget zone decreased from S$_2$ to S$_1$ by 7.1%, leading to an increase in electrical conductivity. For sample S$_2$, the specific contact resistance is 2.7×10^{-8} Ω m^2, which indicates a decrease in peak temperature during different C-rates compared to S$_1$. Compared with the other two samples, sample S$_3$ exhibits a lower electrical resistivity of 2.87×10^{-5} Ω cm, indicating a small heat generated at different C-rates. The contact resistance of 2.5×10^{-8} Ω m^2 is observed for sample S$_3$. In contrast, the busbar with Cu-rich IMC is highly conductive and generates a small heat, resulting in decreased thermal failures while charging and discharging the battery pack.

Table 5. Variation of the electrical resistivity and specific contact resistance from experimental and simulations study, respectively of busbars

Sample nomenculature	Experimental electrical resistivity ($\times 10^{-5}$ Ω cm)	Simulation specific contact resistance ($\times 10^{-8}$ Ω m^2)
S_1	4.29	3
S_2	3.44	2.7
S_3	2.87	2.5

In addition to the IMC effect on C-rate, the pulse charge-discharge voltage curves of the Li-ion cell have been examined. Figure 4e illustrates voltage versus time for different busbars operating at varying C-rates. The voltage is measured between the cell and the attached busbar, and the busbar composition significantly affects the voltage drop. An initial battery voltage of 3.35V is subjected to 1C-rate discharge. The voltage drop for the samples S_1, S_2, and S_3 is observed to be 0.1 V, 0.08 V, and 0.06 V, respectively. Observations have shown that the sample with high electrical resistivity has observed high voltage drops. Figure 4e shows that voltage drop increases with an increase in C-rate from 1 to 2.

As discussed in the previous section, an increase in C-rate results in increased heat generation in the battery and busbar. Temperature dependence can also be associated to open circuit voltage (OCV) at a common time point following the discharge of a Li-ion battery at various discharge rates without changing the initial voltage. The OCV of an Li-ion battery is also determined by measuring the current and voltage responses during charge and discharge. Moreover, the OCV is a key characteristic of Li-ion batteries. It measures ionized energy changes within electrodes and battery state of charge (SoC = 1-DoD). The variation in the OCV is negligible at a lower C-rate as it increases and the OCV decreases. The OCV of all samples of the busbar is ~3.29 V at 1C-rate. At 1.5C-rate, the OCV values for samples S_1, S_2, and S_3 are 3.24 V, 3.26 V, and 3.28 V, respectively. A higher OCV has a higher 1-DoD percentage and greater cell capacity. Additionally, when the C-rate is increased to 2, the OCV decreases, and sample S_1 had an OCV of 3.12V, which is 0.12 V smaller than the 1C-rate determines the degradation of cell capacity. Meanwhile, sample S_3 showed a decrease of 0.03V in comparison to the 1C-rate. In conclusion, S_3 has a higher 1-DoD percentage and greater cell capacity than other samples.
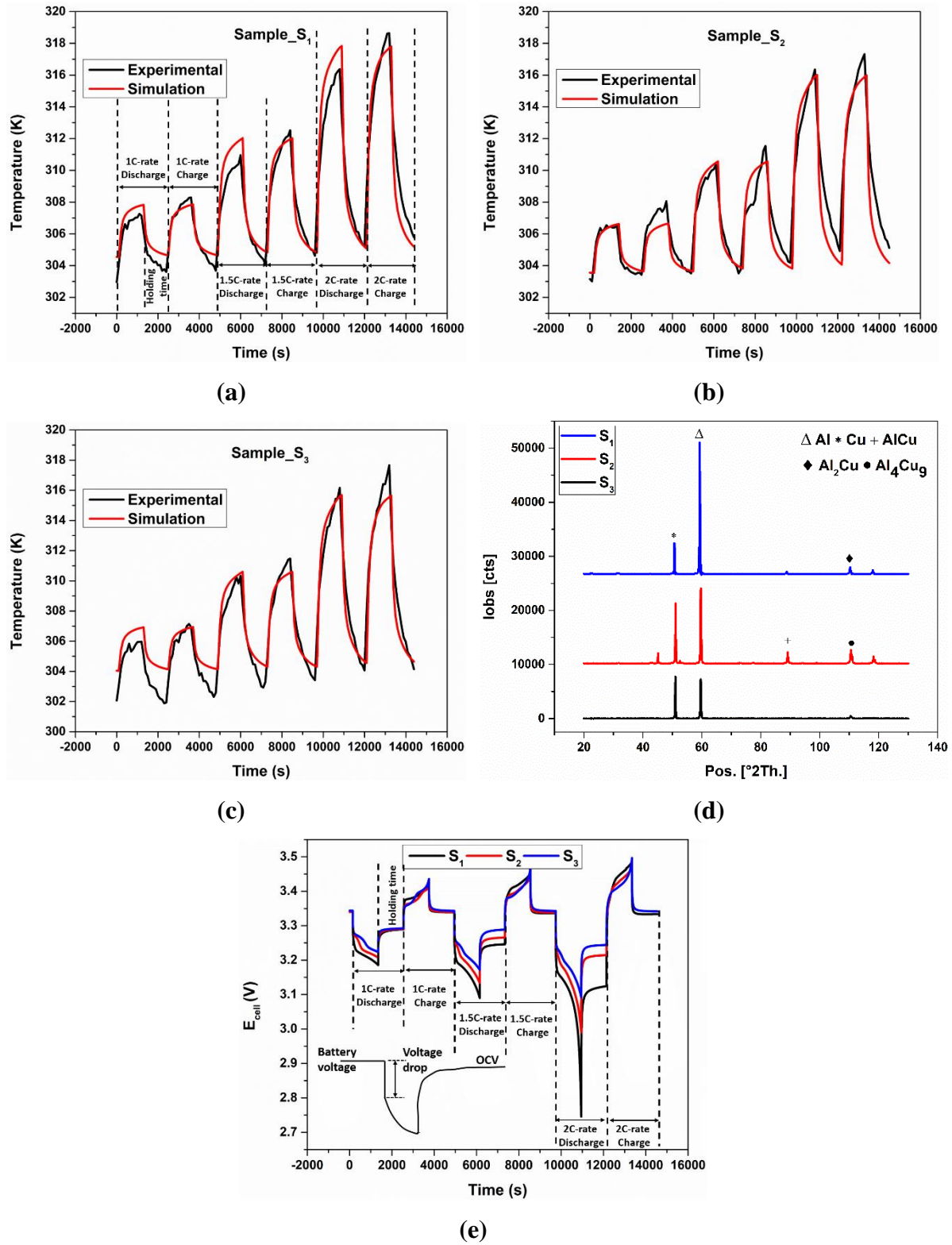
Figure 4. The time versus temperature plots measured at the joint interface of the busbar samples (a) S_1, (b) S_2, (c) S_3, (d) XRD patterns at the weld nugget zone, and (e) the pulse charge-discharge voltage curves

4.2 Microstructural analysis

The Al-Cu busbar was subjected to EBSD to determine the grain size, grain misorientation angle, plastic deformation, and texture. As shown in Figures 5a, b, and c, EBSD mapping of the busbar has been validated using image quality (IQ) maps. The inverse pole Figure (IPF) maps in Figures 5d, e, and f show grain refinement in the busbar after FSW. A grain boundary misorientation map of the specimens in Figures 5g, h, and i, is superimposed over IQ maps in Figures 5a, b, and c. The red, green, and blue lines indicate low angle grain boundaries (LAGBs) with misorientations between 2° and 15°, high angle grain boundaries (HAGBs) with misorientations greater than 15°, and twin boundaries (TBs). Due to the cubic structure, Cu has a maximum misorientation angle value of 62.8°.

(a) (b) (c)

(d) (e) (f)

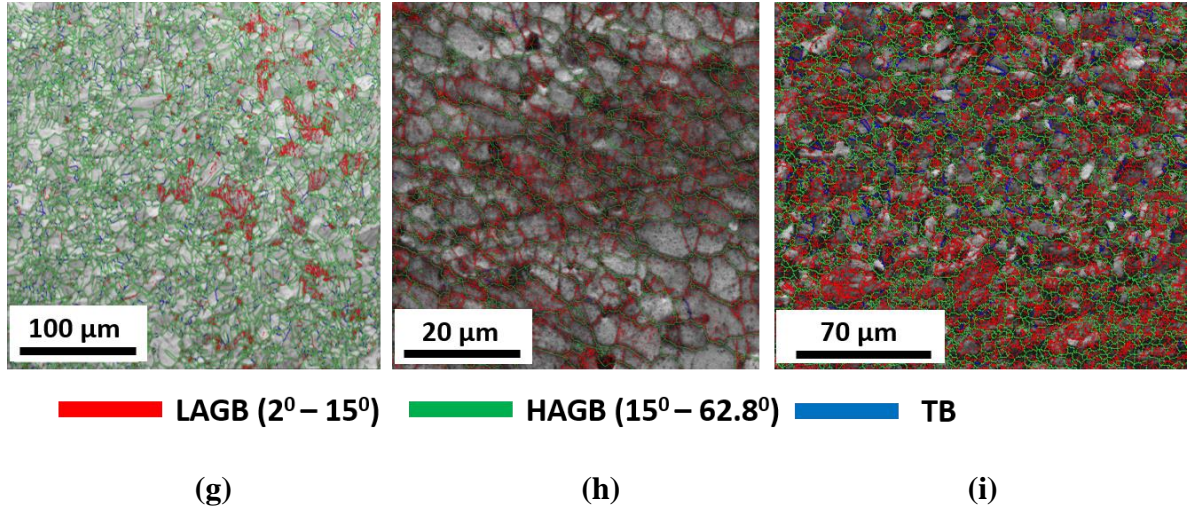**(g)**   **(h)**   **(i)**
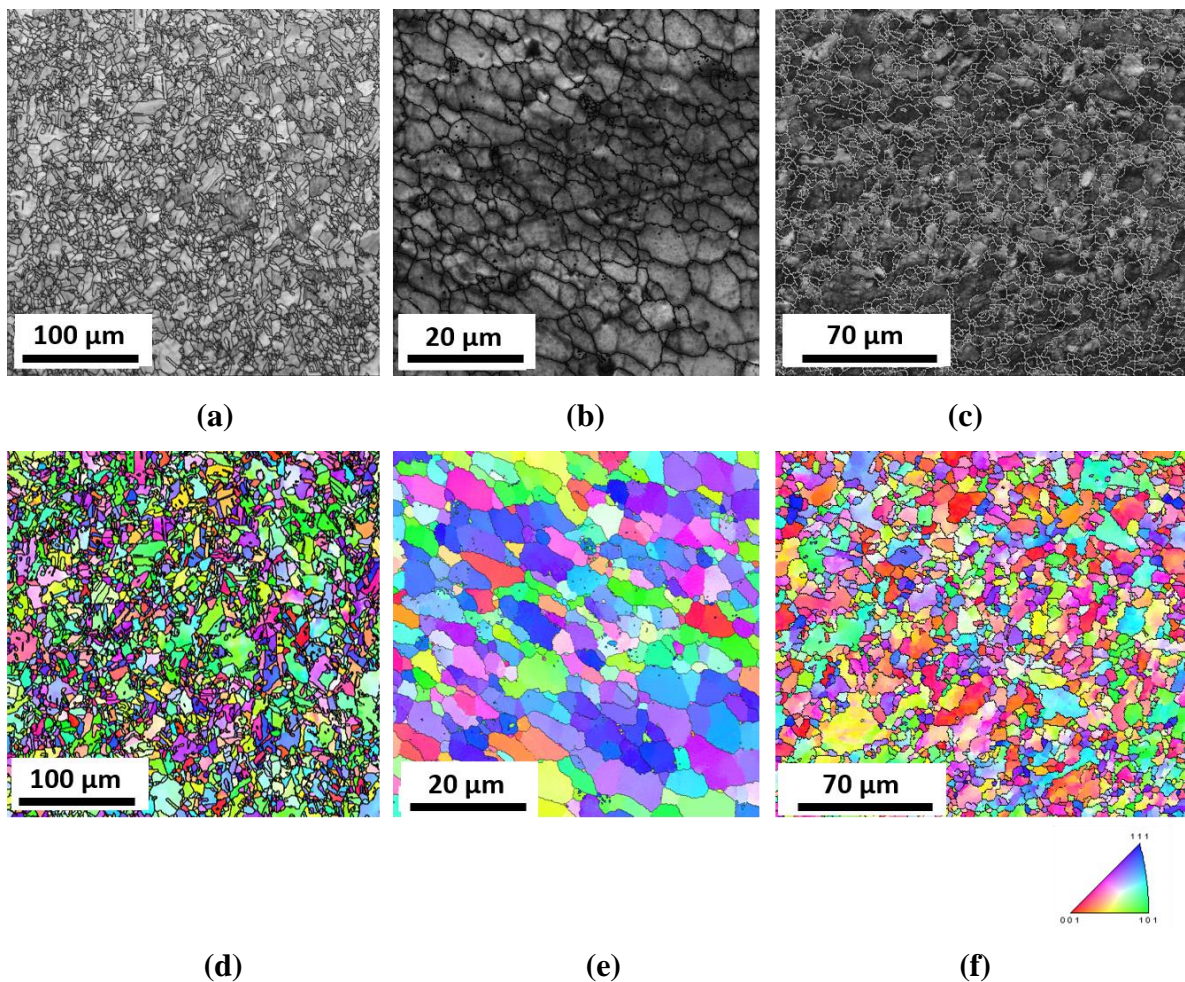
Figure 5. The EBSD analysis of busbar obtaining IQ, IPF, and grain boundary misorientation superimposed IQ maps for sample, (a)-(d)-(g) S_1, (b)-(e)-(h) S_2, and (c)-(f)-(i) S_3, respectively

The NZ of the FSWed specimen has refined grains with nearly equiaxed microstructure, as observed from Figures 5d, e, and f. The average grain size in NZ of the samples S_1, S_2, and S_3 are 4.92 µm, 8.67 µm, and 7.85 µm, respectively. A reduction in grain size indicates an increase in GB. Because the GBs are disordered and amorphous, they disrupt the crystal structure. GBs with a high amount of defects will block carrier transitions, increasing electrical resistivity. Material with a thicker grain boundary has more disordered atoms. In consequence, Al-Cu busbars have a higher resistivity due to their reduced grain sizes and substantial increase in GB. The stirring action caused by the FSW tool causes frictional heat, leading to significant deformation at the NZ. The increase in rotational speed of the tool increases the heat generation, which leads to enhanced grain misorientation and intensified plastic strains. Figures 5g, h, and i show the distribution of misorientation angles also show that LAGB increases with an increase in rotational speed, i.e., LAGB increases from 14.9 % to 65.8 % from sample S_1 to S_2. With the increase in welding speed, the LAGB decreases to 46.2 % for S_3. LAGB increases as the original coarse grains refine into a small grains and sub-grains due to a temperature rise. Similarly, with an increase in rotation speed for samples S_1 and S_2, the TB decreases from 42.3 % to 1.2 % in NZ due to dynamic recrystallization. In response to high strain rate plastic deformations, grain refinement occurs at higher rotational speeds due to the formation of sub-grains and newly nucleated grains through recrystallization, recovery, or grain breakdown. Due to the deformation, the density of dislocations increases, creating sub-grains, creating higher LAGB percentages [43], and decreasing TB percentages. Further, as the welding speed increases, grain growth may occur during fast cooling, which increases the TB fraction.

However, GB defects and GB energy decreased with increasing twin density. The reduction in twin density increases electrical resistivity [44].

4.3 Busbar behaviour at higher C-rates

In order for EVs' to be more environmentally friendly and convenient than conventional internal combustion engines, the charging must occur at higher power rates to decrease the charging time while at the same time ensuring that the battery pack operates for a maximum amount of time. However, technical limitations exist at each stage of the process: batteries heat up during charging due to internal resistance inside the cell and also between mechanical components. As the temperature increases, the battery pack may suffer from several thermal failures that would reduce its efficiency. Figures 6 and 7 show temperature contour on the Li-ion cell and the busbar at the 5 and 10C-rate. For a specific contact resistance of 2.5 10⁻⁸, the maximum temperature recorded at the li-ion cell and the busbar during discharge for 5C-rate is 322.0 K and 354.4 K, respectively. For a 10C-rate, the maximum temperature recorded in the cell is 367.5 K, while that in the busbar was 514.3 K. Similarly, the corresponding temperature contours for other specific contact resistances has been depicted in Figs 6 and 7.
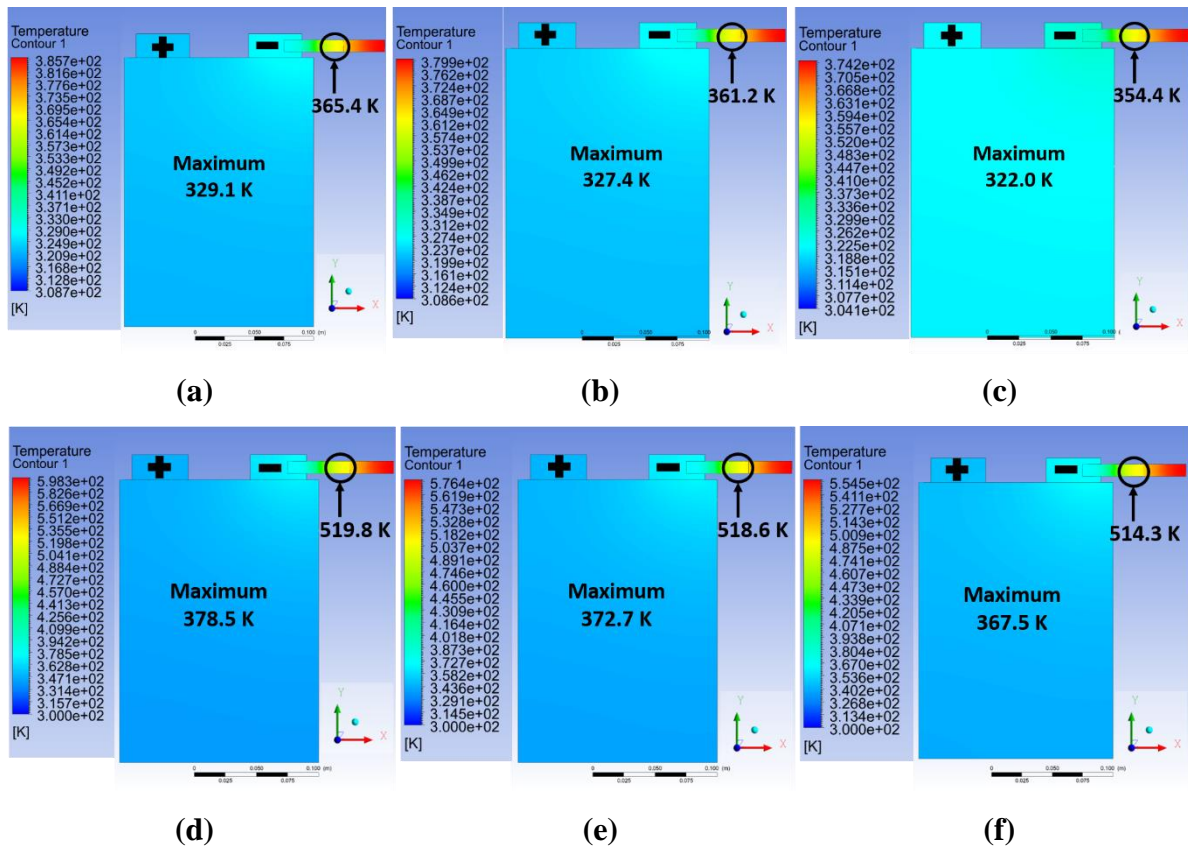

(a)   (b)   (c)

(d)   (e)   (f)

Figure 6. Temperature contours of Li-ion cell clamped with busbar during discharge state for sample S_1, S_2, and S_3 (a)-(b)-(c) 5C-rate, (d)-(e)-(f) 10C-rate, respectively

At higher C-rates, the temperature rise may cause external or internal thermal short-circuits. External short-circuits may cause the failure of the busbar and other electronic components, while internal short-circuits may lead to failure of the Li-ion cell [45]. Thus, it was concluded that for higher C-rates, such as 5C-rate and 10C-rate, a cooling system has to be deployed to prevent various problems like electrolyte decomposition, solid electrolyte interphase breakdown, and thermal failures, respectively.
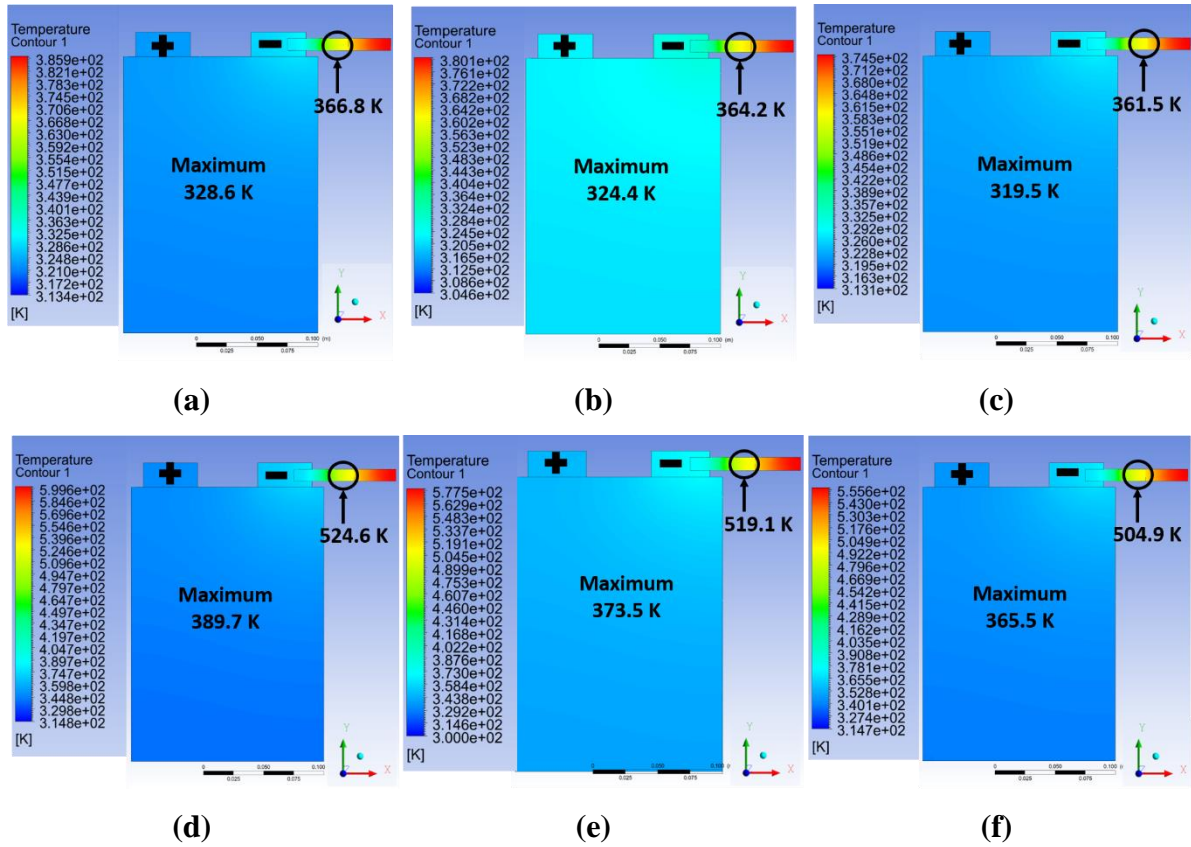

(a)   **(b)**   **(c)**

(d)   **(e)**   **(f)**

Figure 7. Temperature contours of Li-ion cell clamped with busbar during charge state for sample S_1, S_2, and S_3 (a)-(b)-(c) 5C-rate, (d)-(e)-(f) 10C-rate, respectively

5. Conclusion

The Al-Cu busbar is successfully fabricated using the FSW for improved mechanical, metallurgical, and electrical properties. In the present study, the FSW busbar is attached with a Li-ion cell and subjected to different C-rates. A similar Li-ion cell attached with a busbar is

modelled to obtain the specific contact resistance between the Al and Cu joints. The specific contact resistance is further used to simulate the Li-ion battery system at higher C-rates. Based on these experimental and simulation conditions, the following conclusions are drawn.

1) The temperature contour from the simulation during different C-rates is validated with an accuracy of ~98.5% based on experimental results, and specific contact resistance is found to be $3 \times 10^{-8}\,\Omega\,m^2$, $2.7 \times 10^{-8}\,\Omega\,m^2$ and $2.5 \times 10^{-8}\,\Omega\,m^2$ for the samples S_1, S_2, and S_3, respectively from the simulation result.

2) The busbar with higher hardness, i.e., small grain size at the weld interface, has smaller electrical conductivity due to an increase in the grain boundary defects. Thus, the sample S_3 had a microhardness of 238 HV and a grain size of 7.85 μm, resulting in a smaller electrical resistivity of $2.87\ 10^{-5}\,\Omega$ cm.

3) The busbar with Al-rich (Al_2Cu) IMC exhibits bad electrical properties with an electrical resistivity of $4.29\ 10^{-5}\,\Omega$ cm, which is 33.1 % higher resistive than the Cu-rich (Al_4Cu_9) IMC.

Additionally, these promising results can be used to simulate the entire battery pack with the effective, i.e., Cu-rich IMC FSW busbar to increase the efficiency of the battery pack. In addition, a suitable cooling system can be designed based on the maximum temperatures obtained at higher C-rates during the simulation.

Credit authorship contribution statement

Omkar Mypati: Writing – original draft, Methodology, Experimentation, Validation, Formal analysis, Investigation, Visualization. **Tariq Anwaar:** Writing – original draft, Methodology, Software, Validation. **Desham Mitra:** Writing – review & editing, Methodology, Experimentation. **Surjya Kanta Pal:** Writing – review & editing, Methodology, Resources, Supervision. **Prakash Srirangam:** Writing – review & editing, Supervision.

Declaration of competing interest

The authors declare that they have no known competing financial interests or personal relationships that could have influenced the work reported in this paper.

References

[1]   R.D. Reitz, H. Ogawa, R. Payri, T. Fansler, S. Kokjohn, Y. Moriyoshi, A.K. Agarwal, D. Arcoumanis, D. Assanis, C. Bae, K. Boulouchos, M. Canakci, S. Curran, I. Denbratt, M. Gavaises, M. Guenthner, C. Hasse, Z. Huang, T. Ishiyama, B. Johansson, T. V. Johnson, G. Kalghatgi, M. Koike, S.C. Kong, A. Leipertz, P. Miles, R. Novella, A. Onorati, M. Richter, S. Shuai, D. Siebers, W. Su, M. Trujillo, N. Uchida, B.M. Vaglieco, R.M. Wagner, H. Zhao, The future of the internal combustion engine, Int. J. Engine Res. 21 (2020) 3–10. https://doi.org/10.1177/1468087419877990.

[2]   F. Zhao, K. Chen, H. Hao, Z. Liu, Challenges, potential and opportunities for internal combustion engines in China, Sustain. 12 (2020) 1–15. https://doi.org/10.3390/su12124955.

[3]   J. Becker, T. Nemeth, W. Raphael, S. Dirk, Uwe, Dimensioning and Optimization of Hybrid Li-Ion Battery Systems for EVs, World Electr. Veh. J. 9 (2018). https://doi.org/10.3390/wevj9020019.

[4]   M. Pfriem, F. Gauterin, EVS29 Symposium Development of real-world Driving Cycles for Battery Electric Vehicles, EVS29 Symp. 8 (2016) 14–24.

[5]   R. Faria, P. Moura, J. Delgado, A.T. De Almeida, A sustainability assessment of electric vehicles as a personal mobility system, Energy Convers. Manag. 61 (2012) 19–30. https://doi.org/10.1016/j.enconman.2012.02.023.

[6]   L. Kouchachvili, W. Yaïci, E. Entchev, Hybrid battery / supercapacitor energy storage system for the electric vehicles, J. Power Sources. 374 (2018) 237–248. https://doi.org/10.1016/j.jpowsour.2017.11.040.

[7]   R. Andrea, Aurora, M. Inut, S. Sergiu-Dan, A look into electric/hybrid cars from an ecological perspective, Procedia Technol. 19 (2015) 438–443. https://doi.org/10.1016/j.protcy.2015.02.062.

[8]   A. Das, L. Dezhi, W. David, G. David, Joining Technologies for Automotive Battery Systems Manufacturing, World Electr. Veh. J. 9 (2018) 1–13.

https://doi.org/10.3390/wevj9020022.

[9]   N. Braunovic, Milenko; Konchits.V, Valery; Myshkin. K, Electrical contacts; Fundamentals, applications and technology, CRC Press. Taylor Fr. Gr. 23 (2006) 652.

[10]   M.S.M. Isa, K. Moghadasi, M.A. Ariffin, S. Raja, M.R. bin Muhamad, F. Yusof, M.F. Jamaludin, N. bin Yusoff, M.S. bin Ab Karim, Recent research progress in friction stir welding of aluminium and copper dissimilar joint: a review, J. Mater. Res. Technol. 15 (2021) 2735–2780. https://doi.org/10.1016/j.jmrt.2021.09.037.

[11]   A.I. B231/B231M-16, Standard Specification for Concentric-Lay-Stranded Aluminum 1350 Conductors, (2016) 11. https://doi.org/https://doi.org/10.1520/B0231_B0231M-16.

[12]   M.J. Brand, P. Berg, E.I. Kolp, T. Bach, P. Schmidt, A. Jossen, Detachable electrical connection of battery cells by press contacts, J. Energy Storage. 8 (2016) 69–77. https://doi.org/10.1016/j.est.2016.09.011.

[13]   C. Bolsinger, M. Zorn, K.P. Birke, Electrical contact resistance measurements of clamped battery cell connectors for cylindrical 18650 battery cells, J. Energy Storage. 12 (2017) 29–36. https://doi.org/10.1016/j.est.2017.04.001.

[14]   N. Wassiliadis, M. Ank, L. Wildfeuer, M.K. Kick, M. Lienkamp, Experimental investigation of the influence of electrical contact resistance on lithium-ion battery testing for fast-charge applications, Appl. Energy. 295 (2021) 117064. https://doi.org/10.1016/j.apenergy.2021.117064.

[15]   J. Kaspar, M. Zimmermann, A. Ostwaldt, G. Goebel, J. Standfuß, B. Brenner, Challenges in joining aluminium with copper for applications in electro mobility, Mater. Sci. Forum. 783–786 (2014) 1747–1752. https://doi.org/10.4028/www.scientific.net/msf.783-786.1747.

[16]   J.I. Feng, X.U.E. Song-bai, L.O.U. Ji-yuan, L.O.U. Yin-bin, W. Shui-qing, Microstructure and properties of Cu / Al joints brazed with ZníAl filler metals, Trans. Nonferrous Met. Soc. China. 22 (2012) 281–287. https://doi.org/10.1016/S1003-6326(11)61172-2.

[17]   S.J. Lee, H. Nakamura, Y. Kawahito, S. Katayama, Effect of welding speed on microstructural and mechanical properties of laser lap weld joints in dissimilar Al and

Cu sheets, Sci. Technol. Weld. Join. 19 (2014) 111–118.
https://doi.org/10.1179/1362171813Y.0000000168.

[18]   O. Mypati, S.K. Pal, P. Srirangam, A Study on Electrical Conductivity of Micro
Friction Stir-Welded Dissimilar Sheets for Hybrid Electric Vehicles (HEVs), in:
Springer Int. Publ., Springer International Publishing, Cham, 2019: pp. 619–627.

[19]   O. Mypati, P.K. Polkampally, P.I. MD, S. Pal, P. Srirangam, Molecular dynamics
simulation of atomic diffusion in friction stir spot welded Al to Cu joints, Mech. Adv.
Mater. Struct. (2021). https://doi.org/10.1080/15376494.2021.1972188.

[20]   O. Mypati, D. Mishra, S. Sahu, S.K. Pal, P. Srirangam, A Study on Electrical and
Electrochemical Characteristics of Friction Stir Welded Lithium-Ion Battery Tabs for
Electric Vehicles, J. Electron. Mater. (2019). https://doi.org/10.1007/s11664-019-
07711-8.

[21]   W.B. Lee, K.S. Bang, S.B. Jung, Effects of intermetallic compound on the electrical
and mechanical properties of friction welded Cu/Al bimetallic joints during annealing,
J. Alloys Compd. 390 (2005) 212–219. https://doi.org/10.1016/j.jallcom.2004.07.057.

[22]   H. Hinz, Comparison of lithium-ion battery models for simulating storage systems in
distributed power generation, Inventions. 4 (2019).
https://doi.org/10.3390/inventions4030041.

[23]   B. Yann Liaw, R.G. Jungst, A. Urbina, T.L. Paez, Modeling of Battery Life I. The
Equivalent Circuit Model (ECM) Approach, Sandia Natl. Lab. (2003) 6.
http://www.sandia.gov/ess/EESAT/2003_papers/Liaw.pdf.

[24]   M. Chen, G.A. Rincon-Mora, Accurate Electrical Battery Model Capable of
Predicting, IEEE Trans. Energy Convers. 21 (2006) 504–511.

[25]   M. Yu, Y. Li, I. Podlubny, F. Gong, Y. Sun, Q. Zhang, Y. Shang, B. Duan, C. Zhang,
Fractional-order modeling of lithium-ion batteries using additive noise assisted
modeling and correlative information criterion, J. Adv. Res. 25 (2020) 49–56.
https://doi.org/10.1016/j.jare.2020.06.003.

[26]   J. Su, M. Lin, S. Wang, J. Li, J. Coffie-Ken, F. Xie, An equivalent circuit model
analysis for the lithium-ion battery pack in pure electric vehicles, Meas. Control
(United Kingdom). 52 (2019) 193–201. https://doi.org/10.1177/0020294019827338.

[27] J. Xu, B. Liu, X. Wang, D. Hu, Computational model of 18650 lithium-ion battery with coupled strain rate and SOC dependencies, Appl. Energy. 172 (2016) 180–189. https://doi.org/10.1016/j.apenergy.2016.03.108.

[28] M.R. Jongerden, B.R. Haverkort, Which battery model to use?, IET Softw. 3 (2009) 445–457. https://doi.org/10.1049/iet-sen.2009.0001.

[29] M. Petit, E. Calas, J. Bernard, A simplified electrochemical model for modelling Li-ion batteries comprising blend and bidispersed electrodes for high power applications, J. Power Sources. 479 (2020) 228766. https://doi.org/10.1016/j.jpowsour.2020.228766.

[30] Q. Zhang, D. Wang, B. Yang, X. Cui, X. Li, Electrochemical model of lithium-ion battery for wide frequency range applications, Electrochim. Acta. 343 (2020). https://doi.org/10.1016/j.electacta.2020.136094.

[31] K.H. Kwon, C.B. Shin, T.H. Kang, C.S. Kim, A two-dimensional modeling of a lithium-polymer battery, J. Power Sources. 163 (2006) 151–157. https://doi.org/10.1016/j.jpowsour.2006.03.012.

[32] Y. Li, M. Vilathgamuwa, T. Farrell, S.S. Choi, N.T. Tran, J. Teague, A physics-based distributed-parameter equivalent circuit model for lithium-ion batteries, Electrochim. Acta. 299 (2019) 451–469. https://doi.org/10.1016/j.electacta.2018.12.167.

[33] U. Seong Kim, J. Yi, C.B. Shin, T. Han, S. Park, Modeling the Dependence of the Discharge Behavior of a Lithium-Ion Battery on the Environmental Temperature, J. Electrochem. Soc. 158 (2011) A611. https://doi.org/10.1149/1.3565179.

[34] O. Kalkan, A. Celen, K. Bakirci, Experimental and numerical investigation of the LiFePO4 battery cooling by natural convection, J. Energy Storage. 40 (2021) 102796. https://doi.org/10.1016/j.est.2021.102796.

[35] H. Gu, Mathematical Analysis of a Zn / NiOOH Cell, J. Electrochem. Soc. 130 (1983) 1459–1464. https://doi.org/10.1149/1.2120009.

[36] G.H. Kim, A. Pesaran, R. Spotnitz, A three-dimensional thermal abuse model for lithium-ion cells, J. Power Sources. 170 (2007) 476–489. https://doi.org/10.1016/j.jpowsour.2007.04.018.

[37] J. Newman, W. Tiedemann, Potential and Current Distribution in Electrochemical

Cells: Interpretation of the Half-Cell Voltage Measurements as a Function of Reference-Electrode Location, J. Electrochem. Soc. 140 (1993) 1961–1968. https://doi.org/10.1149/1.2220746.

[38]   L. Sols, A. Engineering, Current and Potential Distribution in Parallel Electrodes, 244 (1995) 236–244.

[39]   H. Gu, Mathematical Analysis of a Zn / NiOOH Cell, J. Electrochem. Soc. 130 (1983) 1459–1464. https://doi.org/10.1149/1.2120009.

[40]   O. Kalkan, A. Celen, K. Bakirci, A.S. Dalkilic, Experimental investigation of thermal performance of novel cold plate design used in a Li-ion pouch-type battery, Appl. Therm. Eng. 191 (2021) 116885. https://doi.org/10.1016/j.applthermaleng.2021.116885.

[41]   U.S. Kim, C.B. Shin, C.S. Kim, Effect of electrode configuration on the thermal behavior of a lithium-polymer battery, J. Power Sources. 180 (2008) 909–916. https://doi.org/10.1016/j.jpowsour.2007.09.054.

[42]   U.S. Kim, C.B. Shin, C.S. Kim, Modeling for the scale-up of a lithium-ion polymer battery, J. Power Sources. 189 (2009) 841–846. https://doi.org/10.1016/j.jpowsour.2008.10.019.

[43]   K. Huang, R.E. Logé, A review of dynamic recrystallization phenomena in metallic materials, Mater. Des. 111 (2016) 548–574. https://doi.org/10.1016/j.matdes.2016.09.012.

[44]   X.H. Chen, L. Lu, K. Lu, Electrical resistivity of ultrafine-grained copper with nanoscale growth twins, J. Appl. Phys. 102 (2007) 1–8. https://doi.org/10.1063/1.2799087.

[45]   T. Werling, P. Geuting, P. Höschele, C. Ellersdorfer, W. Sinz, Investigation of the electro-mechanical behavior of automotive high voltage busbars under combined electrical load with varying indenter geometry and environmental conditions, J. Energy Storage. 32 (2020) 101861. https://doi.org/10.1016/j.est.2020.101861.